A multi-phase SPH simulation of hydraulic jump oscillations and local scouring processes downstream of bed sills

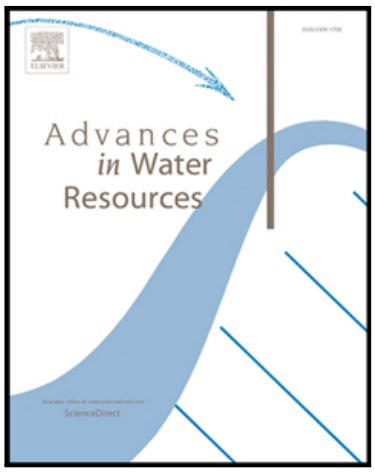

A Multi-phase SPH simulation of Hydraulic Jump oscillations and local scouring processes downstream of bed sills

Diana De Padova , Mouldi Ben Meftah , Michele Mossa , Stefano Sibilla

PII: S0309-1708(21)00248-7
DOI: https://doi.org/10.1016/j.advwatres.2021.104097
Reference: ADWR 104097

To appear in: *Advances in Water Resources*

Received date: 22 June 2021
Revised date: 22 October 2021
Accepted date: 2 December 2021

Please cite this article as: Diana De Padova , Mouldi Ben Meftah , Michele Mossa , Stefano Sibilla , A Multi-phase SPH simulation of Hydraulic Jump oscillations and local scouring processes downstream of bed sills, *Advances in Water Resources* (2021), doi: https://doi.org/10.1016/j.advwatres.2021.104097

Highlights

- A multi-phase SPH sediment-water model is proposed for flow simulation in scour holes;
- Experimental observations have been used for the calibration of an SPH model;
- Detailed physical processes of hydraulic jump flows in a scour hole are investigated

A Multi-phase SPH simulation of Hydraulic Jump oscillations and local scouring processes downstream of bed sills

Diana De Padova[1,2], Mouldi Ben Meftah[1,2], Michele Mossa[1,2], Stefano Sibilla[3]

[1] Polytechnic University of Bari, DICATECh, Bari, Italy

[2] CoNISMa, Inter University Consortium for Marine Sciences, Rome, Italy

[3] Department of Civil Engineering and Architecture (DICAr), University of Pavia

* Corresponding author: diana.depadova@poliba.it

Highlights

- A multi-phase SPH sediment-water model is proposed for flow simulation in scour holes;
- Experimental observations have been used for the calibration of an SPH model;
- Detailed physical processes of hydraulic jump flows in a scour hole are investigated

In the present study, we numerically focus on the vorticity generation mechanism in a scour hole developed downstream of a grade control structure in sand-bed channels. The liquid-granular flow has been simulated through a symplectic Weakly Compressible SPH scheme with a two-equation turbulence model, where the two phases are treated as continua with different rheological properties. The equilibrium configuration of flow field and bed topography is reached after a transient period in which the system oscillates between two flow patterns: (i) the scour hole shows a relatively steep hump downstream of it, increasing the free surface elevation and generating a B-jump type with a counterclockwise rotating macro-vortex structure which pushes the main flow towards the bed, where strong erosive action is observed; (ii) the scour shows a relatively modest inclination of the scour cavity, leading to the formation of a wave jump dominated by a clockwise rotating macro-vortex structure.

Keywords: Smoothed Particle Hydrodynamics; Flow patterns; Scour holes; Hydraulic jump; Local scouring processes.

1. Introduction

Local scour in the vicinity of hydraulic structures is an important phenomenon which may endanger their stability. Therefore, the prediction of the maximum scour depth downstream of hydraulic structures has been widely studied: relevant references can be found for instance in Carstens (1966), Bormann and Julien (1991), Balachandar and Kells (1997), Gaudio et al. (2000), Lenzi et al. (2002), D'Agostino and Ferro (2004), Ben Meftah and Mossa (2006), Martín-Vide and Andreatta (2006), Espa e Sibilla (2014), Manes and Brocchini (2015), Papanicolaou et al. (2018), Wang et al. (2018).

Most of these studies propose prediction formulae for both scour depth and length, which are calibrated on experimental and field data and are made available to designers. The experiments by Ben Meftah and Mossa (2006), Tregnaghi et al. (2007), and Lu et al. (2013) showed that the scour

downstream of a grade control structure evolves into three distinct phases, including an initial phase, a developing phase, and an equilibrium phase.

Experiments by Meftah and Mossa (2006), showed that the extent of the scour hole was strongly dependent on time and observed an initial rapid stage, a progressive stage and a final, decelerated stage. The initial high rate of solid transport was due to the high shear stresses exerted over the sand bed at the initial time. The second stage was characterized by an increased rate of scour development much slower than the first stage. The final slow stage was when the scour achieves equilibrium after a long period of time.

Experiments by Tregnaghi et al. (2007) showed that the scour process usually reaches its equilibrium condition rapidly in live-bed conditions and rather slowly in clear-water conditions. Lu et al. (2013) indicated that the scour hole in non-cohesive sediments depends on the channel bed slope, on the flow conditions, on the densimetric Froude number and on the sediment median size.

However, the complex nature of the local scouring process shows that current knowledge is far from a full understanding of the phenomenon. Whereas most experiments provide measurements at a point or on a plane, the complete flow field supplied by a Computational Fluid Dynamics (CFD) simulation enables the reasearchers to have a deeper understanding of the scouring process. Therefore, CFD methods have become a useful tool to study complex environmental fluid mechanics problems.

The estimation of erosion rates is a key issue for management and long-term operation plans of many hydraulic structures. In a management context, modelling supports the prediction of changes in sediment balance upstream and downstream of a hydraulic structure, with relatively low cost.

In this context, the use of Lagrangian meshless methods appears in general to be particularly suitable for dealing efficiently with the presence of two phases, the combination of interfacial and free-surface flows, in addition to particle entrainment of sediments by the fluid.

Among mesh-free methods, Smoothed Particle Hydrodynamics (SPH) has gained a widespread popularity in the last decades; although it had been initially developed to study astrophysical problems (Gingold and Monaghan, 1977; Lucy, 1977), it has since then been extended to a wide range of engineering applications such as the breaking and impact of waves (Di Monaco et al., 2011; Lin et al., 2015; Makris et al., 2016; Xia and Liang 2016; De Padova et al., 2018a, 2020a), hydraulic jumps (López et al., 2010; Federico et al., 2012; De Padova et al., 2017, 2018b-c; Jonsson et al., 2016), multi-phase flows and fluid–structure interaction (FSI) problems (Pu et al., 2013; Xie and Jin 2016; De Padova et al., 2020b; 2021; Calderon-Sanchez et al., 2021), oscillating jets that induce breaking waves (Espa et al., 2008; De Padova, 2019, 2020c; Barile, 2020) wastewater treatment (Meister and Rauch, 2016); simulation of landslides (Manenti et al., 2016; Ran et al., 2015).

During the last decade, multi-phase SPH numerical studies on sediment transport have been carried out by Manenti et al. (2012), Zanganeh et al. (2012), Ran et al. (2015), Fourtakas and Rogers, (2016) Fu and Jin, (2016), Khanpour et al. (2016), Pahar and Dhar, (2017), Shi et al., (2017), Ulrich et al., (2013), Wang et al. (2018), Zubeldia et al. (2018), Bertevas et al. (2019), Zheng et al. (2019).

In Manenti at al. (2012), both liquid and granular materials were modelled as weakly compressible viscous fluids, whose motion results from the numerical solution of the continuity and momentum equations discretized according to a standard SPH formulation. Comparison with experimental results showed that the eroded volume and the profile evolution were better reproduced by the Shields' criterion. Zanganeh et al. (2012) applied a two-phase SPH method for simulating scour processes beneath a marine pipeline with respect to the sediment and fluid phase interactions. Here, the sediment and fluid phases were described as a non-Newtonian and Newtonian fluid, respectively, and a Sub-Particle Scale (SPS) model was used to represent turbulent stresses.

Ulrich et al. (2013) applied a two-phase SPH method to complex, full-scale marine-engineering problems, including the scouring of sea-port bottom soil due to ship-propeller induced flows. Here, the soil phase was treated as a viscous material with a variable viscosity adhering to the Mohr–Coulomb yield-stress criterion for granular materials, and the constitutive model was supplemented by a suspension treatment to capture the viscosity transition along the water–soil interface. In Ran et al. (2015), an Incompressible SPH (ISPH) erosion model was developed to investigate the sediment

bed scour and grain movement under a dam break flow. The sediment bed erosion model was based on the concept of pick-up flow velocity and the sediment was initiated when the local flow velocity exceeded a critical value.

In Fourtakas and Rogers (2016), the numerical SPH scheme was based on the Bingham-type Herschel–Bulkley–Papanastasiou (HBP) model that allows simulating the rheology of the un-yielded and the yielded material without needing to define a maximum value for viscosity. The multi-phase model was calibrated with experimental and 2-D reference numerical models for scour following a dry-bed dam break. In Fu and Jin (2016), a two-phase SPH method based on a rheology model and a higher order viscosity smoothening scheme was used to reproduce the open channel flow scouring and water–sediment dam break flow.

In Khanpour et al. (2016), a two-phase SPH based on Mohr–Coulomb and Shields yielding criteria, was used to reproduce the scouring downstream of a wall-jet, and a reservoir sediment flushing.

Pahar and Dhar (2017) developed a coupled solenoidal ISPH model for simulation of sediment displacement in erodible bed.

In Wang et al. (2018) a 3D ISPH sediment erosion model was proposed to simulate the scouring process around a large vertical cylinder. The model was based on the TWP concept (Wang et al., 2016) and the sediment motion was initiated when the fluid bottom shear stress exceeded the critical value.

In Zubeldia et al. (2018), a two-phase SPH method based on the Shields criterion and applied to the flow of a two-phase liquid sediment mixture, was employed to model the scouring flows with large deformations.

In Luo and Kazemi (2019), a SPH sediment model was used to study the dynamic hydraulic jump in steep open channels. In Bertevas et al. (2019), a SPH formulation of the classical two-phase mixture model was used to study the turbulent sediment transport and the sediment disturbances generated by moving equipment operating near or on the seabed. The rheological behaviour of clay sediment/water mixtures was modelled using a volume fraction, shear rate-dependent viscosity which accounts for the existence of a yield stress.

In general, some SPH approaches consider the sediment as a single-phase moving mass; other approaches model the sediment as a two-phase mixture, where the voids of the solid matrix are filled by a liquid phase, in order to account for the pressure effect.

However, in all these approaches the basic idea is to model the sediment dynamics like a pseudo-fluid one, once the onset of sediment particle motion is attained. As a result, a criterion that represents the critical condition for the incipient motion of sediment must be defined; this can be done in terms of the critical velocity (Hayashi et al., 2003; Ran et al., 2015) or the critical shear stress (Manenti et al., 2012). In some of the considered works, a numerical threshold was used for this purpose and therefore it is evident that the prediction capability of the model depends on the calibration made. To overcome this limitation, a WCSPH formulation of a mixture model consistent with the kinetic theory of dense granular flows (KTGF), was introduced by Amicarelli et al. (2017), showing a suitable degree of accuracy.

The reader can refer to Manenti et al. (2019) for a comprehensive review of the studies on multi-phase SPH erosion models.

Starting from the research experiences described above, the main aim of this study is to exploit the features of the SPH method, i.e. its inherent ease in the treatment of different rheologies as well as of rapidly varying free surfaces and interfaces, to investigate the effect of sediment movement under the action of rapid flows, such as the ones occurring downstream of a bed sill, which lead to the formation of unsteady hydraulic jumps and evolving scour holes.

To reach this goal, an existing SPH model which has proven to be highly effective in the description of unsteady free-surface flows dominated by turbulence and wave breaking (see e.g. Espa et al., 2008; De Padova et al., 2013, 2018b and 2020a) was extended to include the treatment of soil-water interaction. Among the different available models, the one developed by Ulrich et al. (2013) has been considered suitable because of its peculiar two-phase approach, which takes into account the granular bed as a separate granular phase but treats the water/sediment suspension as a

single fluid phase with variable viscosity. The calibration of the SPH model has been performed by comparing experimental and numerical observations of the local scour holes downstream of a hydraulic jump. Finally, SPH simulations have been used (i) to inspect and detail the vorticity field, evaluating, in particular, its temporal evolution; (ii) to relate the vorticity field and the scour process; (iii) to relate the vorticity field and the free surface dynamics, in particular to the flow surface-parallel deceleration and (iv) to study the temporal evolution of the dominance of vorticity and strain.

2. SPH Numerical method

The liquid-granular flow has been simulated through a SPH approach, where the two phases, treated as continua with different physical and rheological properties, are represented by different sets of particles and no transfer of mass is allowed from one phase to the other. Time advancement is obtained through a symplectic Weakly Compressible SPH (WCSPH) scheme, where artificial compressibility is introduced to solve explicitly in time the equations of motion of the two incompressible fluids.

The motion of both continuum phases is represented by the Navier–Stokes equations, which take the following SPH semi-discrete form:

$$\begin{cases} \left\langle \frac{\mathrm{D}\rho_i}{\mathrm{D}t} \right\rangle = \sum_{j=1}^{N_i} m_j (\boldsymbol{v}_i - \boldsymbol{v}_j) \cdot \widehat{\nabla} W_{ij} \\ \left\langle \frac{\mathrm{D}\boldsymbol{v}_i}{\mathrm{D}t} \right\rangle = -\sum_{j=1}^{N_i} m_j \left(\frac{p_i}{\rho_i^2} + \frac{p_j}{\rho_j^2} \right) \nabla W_{ij} + \sum_{j=1}^{N_i} \frac{m_j}{\rho_j} (\mathcal{T}_i - \mathcal{T}_j) \cdot \widehat{\nabla} W_{ij} + \mathbf{g} \\ p_i - p_0 = c_i^2 (\rho_i - \rho_0) \\ \mathcal{T}_i = \eta_i \mathcal{S}_i \end{cases} \quad (1)$$

where *Wij* represents the C2 Wendland kernel function (Wendland, 1995) evaluated at the interparticle distance and defined over a circle having a radius double than the smoothing length *h*. SPH particle approximation is indicated by angled brackets and is written for each particle *i* having mass m_i. The summations in (1) are extended to all the N_i particles *j* located at a distance smaller than 2*h* from particle *i*, irrespective of the material characterizing the particles.

In Equation (1), $\mathbf{v} = (u, w)$ is the velocity vector, p is pressure, ρ is density, g is the gravity acceleration vector, $\mathcal{T}$ is the shear stress tensor, c is the speed of sound in the weakly compressible fluid, η is a suitable viscosity coefficient, $\mathcal{S}$ is the rate-of-strain tensor and the subscript 0 denotes a reference state for pressure computation. The way in which the viscosity coefficient is evaluated defines the different models which represent the flow of the two phases.

The tilde notation $\widehat{\nabla} W_{ij}$ indicates that the gradient of W_{ij} is renormalized by enforcing 1st order consistency on the 1st derivatives (Sibilla, 2015), leading to a 2nd-order accurate discretization scheme in space. The kernel renormalization is applied to all of the terms in (1), apart from the pressure gradient term, where the form originally proposed by (Monaghan, 1992) is retained to guarantee momentum conservation.

Turbulent liquid flow

In the case of a turbulent flow of the liquid phase, all variables in (1) are assumed to be Reynolds-averaged and the equations of motion become the Reynolds-averaged (RANS) equations. In this case, η represents the kinematic eddy viscosity, which is evaluated through a standard k-ε turbulence model (Launder and Spalding, 1974) as $\eta = c_\mu \frac{k^2}{\varepsilon}$, where k is the turbulent kinetic energy and ε the turbulent dissipation rate.

In the same SPH semi-discrete form as (1), the equations for the turbulence model are (De Padova et al, 2016):

$$\frac{Dk_i}{Dt} = P_{k_i} + \frac{1}{\sigma_k}\sum_{j=1}^{N_i} m_j \frac{\eta_i + \eta_j}{\rho_i + \rho_j}\frac{k_i + k_j}{r_{ij}^2 + 0.01h^2}\boldsymbol{r}_{ij}\cdot\nabla\widehat{W}_{ij} - \varepsilon_i$$
$$\frac{D\varepsilon_i}{Dt} = C_{\varepsilon_1}\frac{\varepsilon_i}{k_i}P_{k_i} + \frac{1}{\sigma_\varepsilon}\sum_{j=1}^{N_i} m_j \frac{\eta_i + \eta_j}{\rho_i + \rho_j}\frac{\varepsilon_i + \varepsilon_j}{r_{ij}^2 + 0.01h^2}\boldsymbol{r}_{ij}\cdot\nabla\widehat{W}_{ij} + C_{\varepsilon_2}\frac{\varepsilon_i}{k_i}\sum_{j=1}^{N_i}\frac{m_j}{\rho_j}\varepsilon_j\widehat{W}_{ij} \quad (2)$$

where P_k is the production of turbulent kinetic energy depending on the local rate of deformation and the model constants have the following values: $\sigma_k = 1$, $\sigma_\varepsilon = 1.3$, $C_{\varepsilon 1} = 1.44$, $C_{\varepsilon 2} = 1.92$.

Granular and suspension flow

Following Ulrich et al. (2013), the granular phase is treated as a viscous material, with a variable viscosity which takes into account also the viscosity transition in the layer where the granular material is found in suspension inside the liquid flow.

The concentration of the suspension is estimated through SPH interpolation as:

$$c_i = \sum_{j=1}^{Ng_i}\frac{m_j}{\rho_j}\widehat{W}_{ij} / \sum_{k=1}^{N_i}\frac{m_k}{\rho_k}\widehat{W}_{ik} \quad (3)$$

where N_{g_i} are the particles of granular material surrounding particle *i*. For a concentration $c_i = 1$, the viscosity of the granular material is computed according to the Mohr-Coulomb yield stress criterion:

$$\eta_i^{MC} = \min\left(\eta_{max}, \frac{\chi\cos\phi + p_i\sin\phi}{\rho_g\|\mathcal{S}_i\|}\right) \quad (4)$$

where χ is the cohesion, φ the friction angle and η_{max} an upper threshold for viscosity to avoid the singularity which occurs when the strain-rate vanishes.

The viscosity of the suspension is derived from the assumption of a constant friction coefficient, which yields:

$$\eta_i^S = \min\left(\eta_{max}, \frac{c_f v_i^2}{\|\mathcal{S}_i\|}\right) \quad (5)$$

A constant value $c_f = 0.01$ is assumed for the friction coefficient, within the range suggested by Fraccarollo and Capart (2002). To smooth the transition between the different layers, the viscosity values are piecewise linearly interpolated between the turbulent eddy viscosity, the suspension viscosity η^S and the granular viscosity η^{MC}, according to the local value of the concentration (3):

$$\eta_i = \begin{cases} c_\mu\frac{k_i^2}{\varepsilon_i} + \frac{\eta_i^S - c_\mu\frac{k_i^2}{\varepsilon_i}}{c_1}c_i & \text{for } 0 \le c_i < c_1 \\ \eta_i^S & \text{for } c_1 \le c_i \le c_2 \\ \eta_i^S + \frac{\eta_i^{MC} - \eta_i^S}{(c_3 - c_2)}(c_i - c_2) & \text{for } c_2 < c_i < c_3 \\ \eta_i^{MC} & \text{for } c_3 < c_i \le 1 \end{cases} \quad (6)$$

For the boundary values between the different viscosity regions, the same values suggested by Ulrich et al. (2013) were adopted, i.e. $c_1 = 0.3$, $c_2 = 0.6$ and $c_3 = 0.99$.

It must be noted that the model by Ulrich et al. (2013) is essentially a single-phase model for the suspension, which is treated as a fluid with varying rheological properties dependent on the local

suspended solid concentration. As such, the model does not take into account explicitly the mass fluxes between the bed granular material and the suspended sediment in the water flow. In this sense, it is an approximate model which holds in the hypotheses of solid transport mainly occurring as bed transport and of non-negligible values of the mixture viscosity only occurring in the near-bed layer. Given the fact that the bed material here analysed is a coarse sand, as explained in Section 3, these hypotheses can be accepted.

The semi-discrete system (1) and (2) is integrated in time by a 2nd-order two-stage XSPH explicit algorithm with a pressure smoothing procedure specifically designed for free-surface flows. More details on the adopted SPH scheme can be found in De Padova et al. (2013, 2016).

Inflow boundary conditions are assigned by introducing a $2h$-wide buffer layer upstream of the computational domain, where the required conditions are imposed to particles located between the bed and the water surface. Each inflow particle is then moved at a constant velocity U_c for a time $t_i = 2h/U_c$ and with constant values of turbulent energy and dissipation, until it enters the computational domain where its properties evolve according to equations (1) and (2). The number of entering particles is determined by the inlet water depth h_1 and is regulated in time in order to guarantee the exact mass flow rate at the inlet; k and ε at the inlet are computed according to an average initial turbulence intensity of 1%.

Zero-gradient outflow boundary conditions are imposed to all the quantities but pressure by introducing a second $2h$-wide buffer layer downstream of the computational domain, where the particle velocity, k and ε are kept unchanged. Pressure is instead imposed according to the hydrostatic pressure gradient resulting from the outlet water depth h_2.

3. Numerical Test

3.1 Numerical parameters and validation of the SPH results

The numerical scheme described above, was used to reproduce the local scouring process experimentally observed downstream of the first bed sill, located 2 m downstream of the wooden ramp (Fig. 1).

The experimental flume bottom is covered with uniform sand particles with a nominal diameter d_{50} = 1.8 mm and density ρ = 2650 kg/m^3. The sill height decreases progressively downstream of the wooden ramp, respecting an assigned initial slope S_0 = 0.0086. Table 1 lists the main experimental parameters of the investigated scour process: L is the distance between sills, h_c is the flow depth over the crest of the sill downstream of which the scour hole is measured, U_c is the flow velocity over the sill, z_s is the maximum equilibrium scour depth from the original bed profile, h_s is the flow depth at the position of maximum equilibrium scour depth, $F_{dc} = U_c/(\Delta g d_{50})^{0.5}$ is the densimetric Froude number for the approaching flow over the sill. Further details and discussion of the results of the experiments can be found in Ben Meftah and Mossa (2006) and in Ben Meftah et al. (2020, 2021).

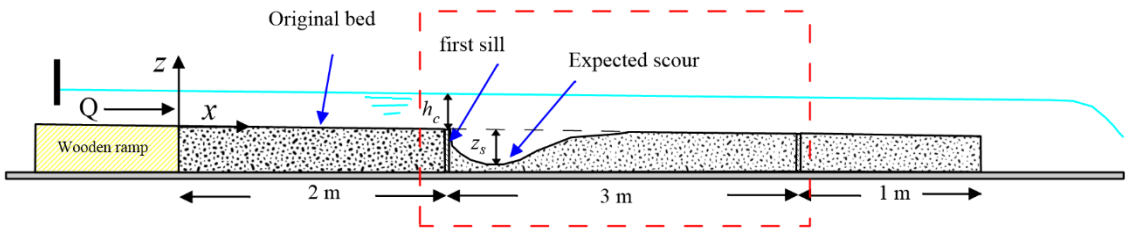

FIG. 1. General sketch of the laboratory flume (Ben Meftah and Mossa, 2006). The dashed rectangle shows the region where the local scouring process has been studied numerically by SPH.

	L (m)	Q (m^3/s)	h_c (m)	U_c (m/s)	z_s (m)	h_s (m)	F_{dc} (-)
T21	3	0.010	0.048	0.686	0.084	0.14	4.019

Table 1: Experimental parameters of the investigated scour process downstream of a bed sill

The numerical domain is 1.2 m long and 0.6 m high, shorter than the laboratory channel. Such a shorter domain was chosen to reduce the computational cost without influencing the quality of the numerical solution, as shown by De Padova et al. (2014). An upstream flow depth $h_1 = h_c = 0.048$ m was therefore chosen, while a flow depth $h_2 = 0.056$ m was imposed downstream. A sketch of the problem setup and of the initial conditions of the SPH simulation can be seen in Figure 2.

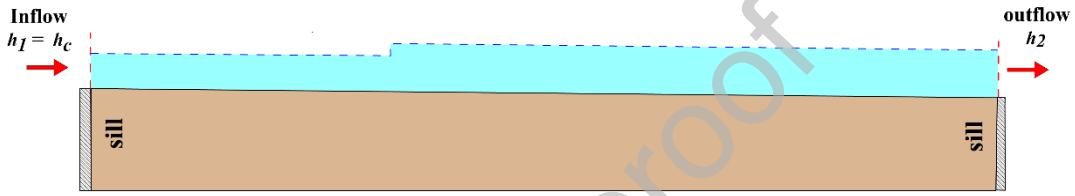

FIG. 2. Geometrical setup and initial conditions.

The efficiency of the SPH kernel function depends also on the choice of the h/Δ ratio, where Δ is the particle spacing: De Padova et al. (2014) showed that a value $h/\Delta \geq 1.2$ should be preferred. Here, the initial particle spacing was taken to be $\Delta = 0.002$ m and a ratio $h/\Delta = 1.5$ was used. The resulting initial number of SPH particles in the simulation was approximately 60,000.

A thorough sensitivity analysis was already performed by the authors in the application of the same SPH numerical method to hydraulic jumps and breaking wave flows (De Padova et al., 2018c, 2019): according to this analysis, the SPH simulations of the cases here studied were performed by adopting a velocity smoothing coefficient in the XSPH scheme $\varphi_v = 0.01$. The simulations were performed with $\chi = 10$ Pa, $\varphi = 41°$ and $\eta_{max} = 0.01$ m²/s in Eq. 4.

The validity of the numerical scheme adopted here was checked against the experimental observations of the local scour holes downstream of hydraulic jumps reported by Ben Meftah and Mossa (2006). The evolution of the scour hole during the SPH simulation is shown, at various time instants, in Fig. 3.

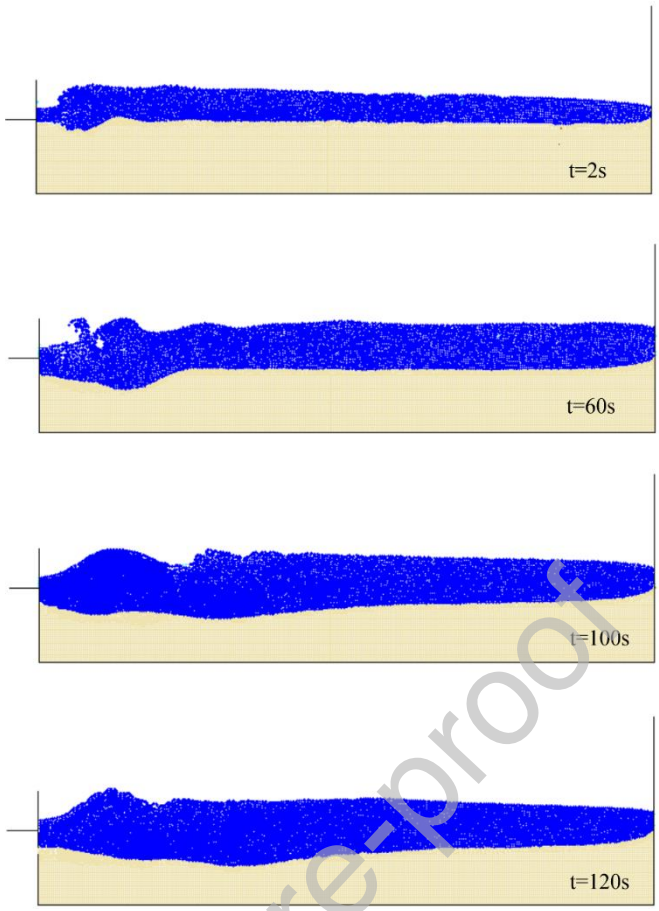

FIG. 3. Snapshots of the SPH simulation at different time instants, highlighting the liquid (blue) and granular (yellow) phases.

Figure 4 shows the resulting SPH and experimental velocity fields superimposed in a vector plot, inside the scour hole downstream of the first bed sill, located 2 m downstream of the wooden ramp. The obtained results highlight that the final model proves to be capable of reproducing the experimental bed evolution, the flow velocity and turbulence intensity through the scour hole. Actually, the three regions which characterize the flow according to the experiments are clearly reproduced; in particular, the flow in region 1, plays a very important role in the initial phase of the scour development. This is due to its high velocity, which leads to an increase of the jet potential erosive action on the bed channel. Region 2 is dominated by a clockwise local vortex at the position of maximum scour depth. In region 3 the velocity vectors tend to be more horizontal. The measured (black dots) and simulated (blue dots) bed profiles at equilibrium are also compared and show a substantial agreement.

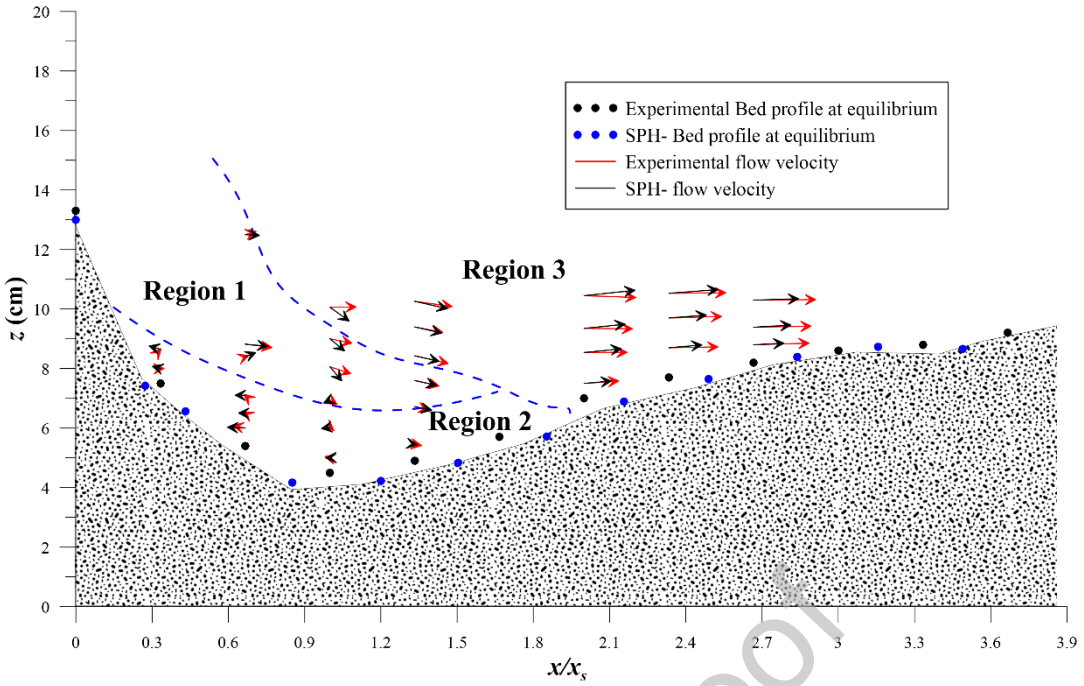

FIG. 4. Vector map of the flow velocity, V_{xz}, in the scour hole at the plane of flow-symmetry (y = 0) (x_s is the x-position from the sill at which the scour attains its maximum depth).

Figure 5 shows the streamwise (U') and the vertical turbulence (W') intensities; U' is defined as the ratio of the standard deviation of the streamwise flow-velocity component fluctuations to the average velocity, $\boldsymbol{U_c}$; W' is defined as the ratio of the standard deviation of the vertical flow-velocity component fluctuation to the average velocity, $\boldsymbol{U_c}$; In the discussion, the fluctuations U' and W' can be considered to be referred to the large-scale fluctuations which are resolved and directly computed by the Lagrangian, time-dependent SPH, while the k-ε turbulence model takes into account also the effect of the modelled small-scale turbulent eddies in a global way, averaging the information on the microscopic turbulence anisotropy.

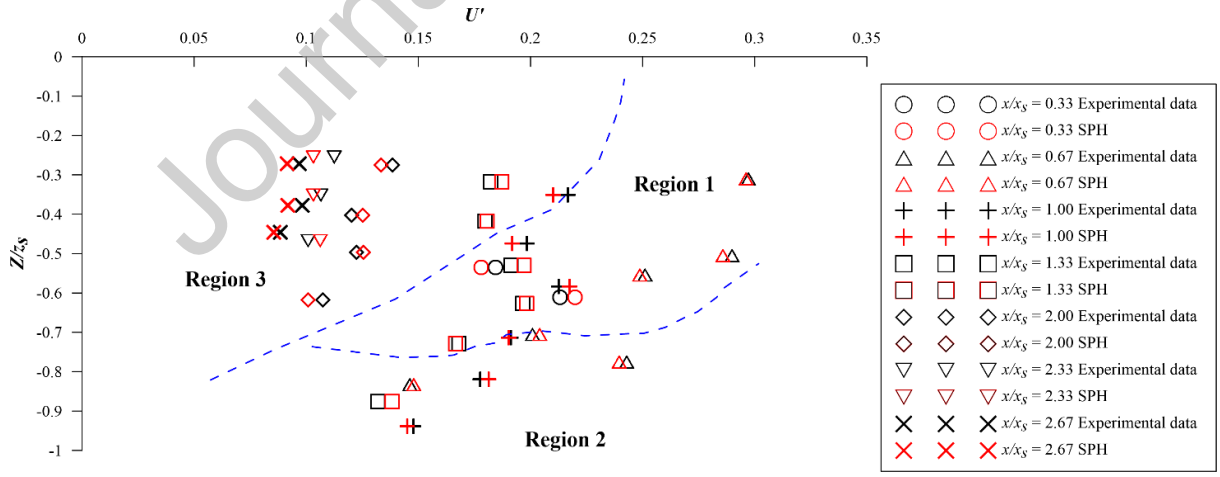

(a)

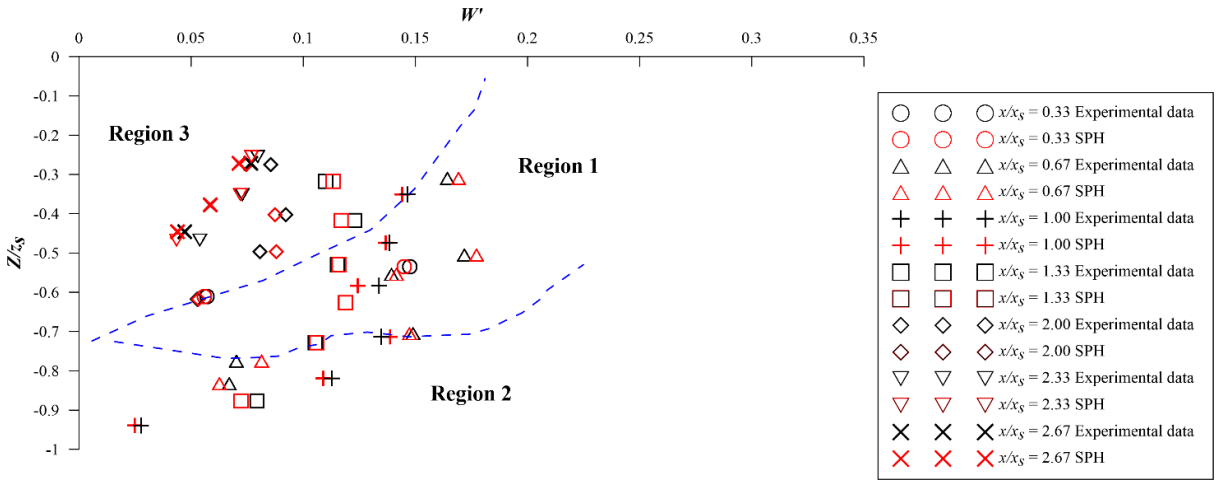

(b)

FIG. 5. Profiles of (a) the streamwise (U') and (b) the vertical turbulence intensities (W') in scour hole at different downstream positions x/x_s. $\boldsymbol{Z}$ is the vertical position from the original bed profile.

The numerical results show that the behavior of the simulated liquid-granular flow is consistent with the experiments of Ben Meftah and Mossa (2006). In particular, the results show that:

(i) the vertical turbulence intensities (W') are smaller than the streamwise ones (U');
(ii) the maximum streamwise (U') and vertical (W') turbulence intensities take place at the regions 1 due to the more intermittent behavior of the jet flow;
(iii) the minimum streamwise (U') and vertical (W') turbulence intensities take place at the region 3 due to the steadier flow velocity distribution;
(iv) in region 2, the streamwise (U') and vertical (W') turbulence intensities show the smallest values comparable to those occurred in region 1, due to the flow velocity reduction;
(v) at the different downstream positions x/x_s, the streamwise (U') and vertical (W') turbulence intensities decrease with decreasing Z/z_s (i.e. approaching the equilibrium-scour bed).

Figure 6 shows the vertical profiles of the time-averaged turbulent kinetic energy, $K = (\langle u'^2 \rangle + \langle w'^2 \rangle)/2$, normalized by $\boldsymbol{U}_c$. Herein, the angle brackets indicate the average over the length of the time series.

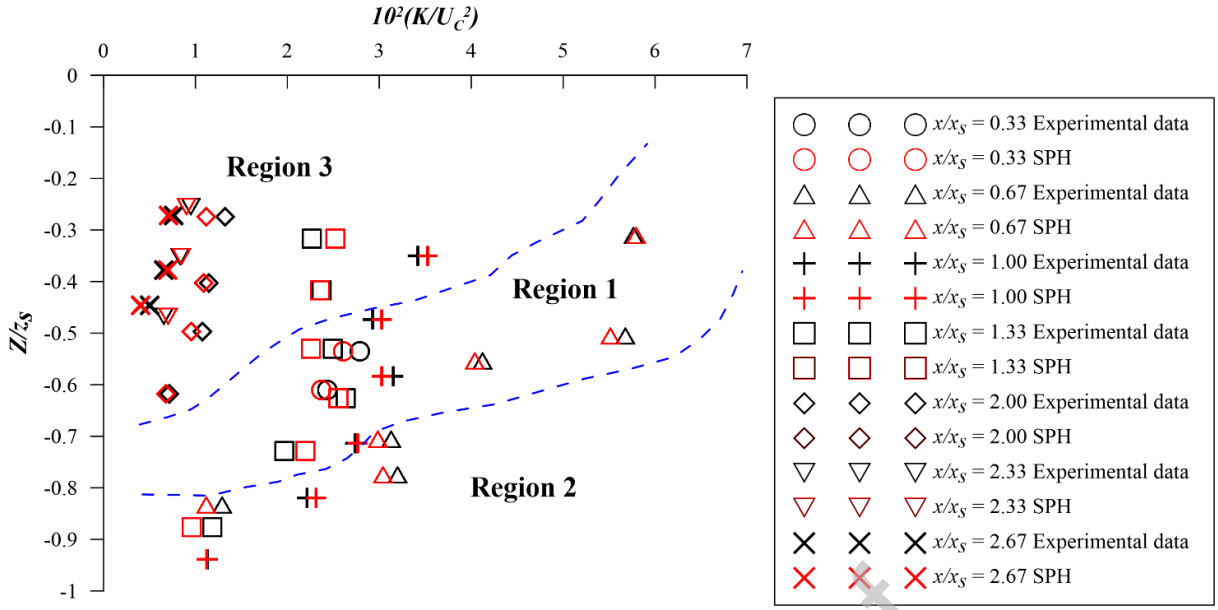

FIG. 6. Vertical profiles of normalized turbulent kinetic energy k/U_c^2 in scour hole at different downstream positions x/x_s

The agreement between the numerical results and laboratory measurements is satisfactory; these results highlight that:

(vi) at all vertical profiles except the one at x/x_s =1.33, the time-averaged turbulent kinetic energy K decreases when Z/z_s decreases (i.e. going down to the equilibrium-scour bed).

(vii) At x/x_s =1.33, the time-averaged turbulent kinetic energy, K, increases when Z/z_s decreases due to the effect of the transition between regions 1 and 3.

To evaluate the model performance, Table 2 shows the statistical analysis of the comparison between the numerical model and the experimental results in terms of the Wilmott index (Wilmott ,1981):

$$I_W = 1 - \frac{\sum_{k=1}^{N}\left(X_{C_k} - X_{m_k}\right)^2}{\sum_{k=1}^{N}\left[\left|X_{C_k} - \overline{X_m}\right| + \left|X_{m_k} - \overline{X_m}\right|\right]^2} \qquad (7)$$

where x_c and x_m are the modelled and measured values of the variable x, respectively, while the bar denotes the average of the modelled and measured values. A perfect agreement between the measured and modelled values is reached when I_W is equal to 1; while a complete discrepancy between numerical and experimental results is observed when I_W tends to 0.

	bed profile	velocity magnitude	velocity direction	turbulence intensities		turbulent kinetic energy
	z_b	$V = \sqrt{u^2 + w^2}$	$\propto = \arctan\left(\frac{w}{u}\right)$	U'	W'	K
I_W	0.90	0.85	0.75	0.89	0.88	0.88

Table 2: Wilmott index for the main variables of the investigated scour process downstream of a bed sill.

Therefore, the SPH model provides a satisfactory prediction in terms of the flow velocity field and the turbulence intensity in the scour holes.

3.2 Flow characterization

Since turbulence is the most important mechanism of sediment entrainment, causing a significant increase in the shear stress around the base of a hydraulic structure, the flow velocity field in the scour holes was analysed. Therefore, in this section, we provide a simple characterization of the flow based both on the vorticity ω and on the Okubo-Weiss parameter W (Okubo, 1970; Weiss, 1991).
Vorticity is defined as:

$$\omega = \left(\frac{\partial u}{\partial z}\right) - \left(\frac{\partial w}{\partial x}\right) \tag{8}$$

and is computed using instantaneous values of the horizontal and vertical velocity.
The W parameter is defined as:

$$W = s_n^2 + s_s^2 - \omega^2 \tag{9}$$

where ω is the vorticity defined by (8), while $s_n = \left(\frac{\partial u}{\partial x}\right) - \left(\frac{\partial w}{\partial z}\right)$ and $s_s = \left(\frac{\partial w}{\partial x}\right) + \left(\frac{\partial u}{\partial z}\right)$ respectively are the normal and shear components of strain rate.

The vorticity maps shown in Fig. 7 were computed from the SPH vector fields. Furthermore, the flow behavior is well described by the instantaneous streamlines representing a single snapshot obtained from the instantaneous velocity field calculated on a regular grid (Fig. 7). Analyzing the results, the equilibrium configuration of flow field and bed topography is reached after a transitory period in which the system oscillates between two flow patterns: (i) at first (Fig. 7(a)), the presence of a scour hole with a relatively steep hump downstream of it leads to an increase of the free surface elevation and to the generation of a B - jump type with a counterclockwise rotating macro-vortex structure (negative vorticity) which pushes the main flow towards the bed, where a strong erosive action is observed and sediments are forced to move downstream. This behavior of the liquid flow is clearly observed by looking at the streamlines, which show that the majority of the flow is oriented parallel to the bed in the downstream direction. However, over the scour hole the streamlines clearly show the flow recirculation and the fluid moving in the upstream direction near the free surface; (ii) later, when the scour hole shows a milder inclination (Fig. 7(b)), the formation of a wave jump is observed. This wave jump is dominated by a clockwise rotating macro-vortex structure (positive vorticity); Here, the clockwise circular motion over the scour hole is clearly shown by the streamlines. The surface boundary layer near the free surface with positive vorticity grows in the downstream direction. Furthermore, there is a concentrated region of negative vorticity near the bed.

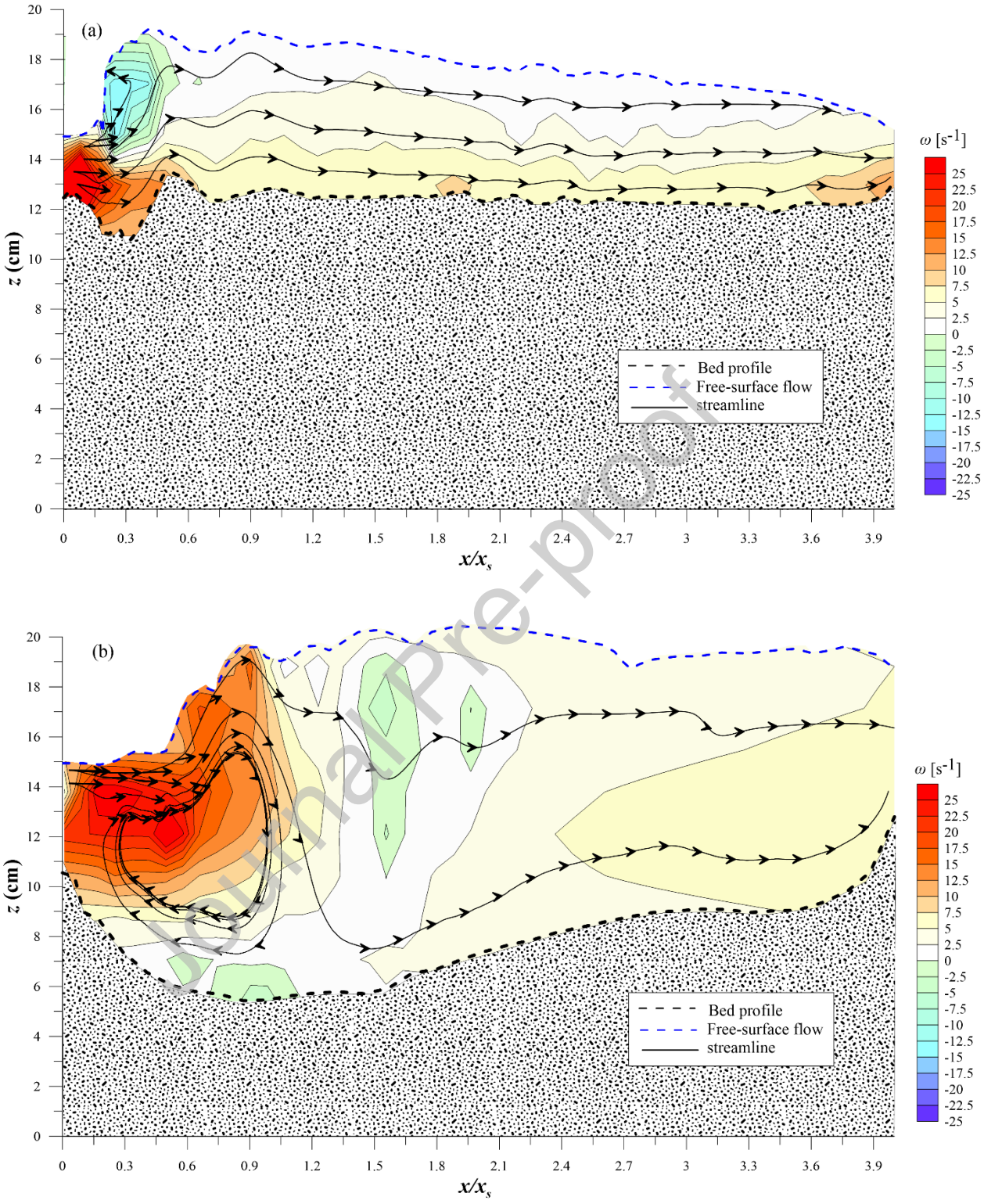

FIG. 7. SPH simulation: Instantaneous values of ω distributions and streamlines at (a) beginning of erosive action (t= 2s) and (b) when the stable configuration has been reached (t= 165s).

The analysis of the vorticity maps alone is not sufficient to identify vortices, since they are masked by background shear. Thus, considering that turbulent structures essentially evolve from interactions between vorticity and strain rate, the maps of the Okubo–Weiss parameter W have been also used to detect coherent structures (Mattioli et al., 2012; Hilt et al., 2020).

Using the local value of W, the flow domain can be partitioned in three distinct types of regions:

(i) vorticity-dominated regions or elliptic regions ($W< 0$);

(ii) strain-dominated regions or hyperbolic regions ($W> 0$);

(iii) Intermediate regions ($W\cong 0$).

Figures 8 and 9 show the comparison between the instantaneous map of ω and of W rated by $W_0=0.2\sigma_W$, with σ_W being the standard deviation of W in the whole domain, at beginning of erosive action ($t= 2$s) and when the stable configuration has been reached ($t= 165$s), respectively.

The map of W/W_0, shown in Figure 8(b), highlights the presence of coherent eddies ($W< 0$) in the near-surface region which is characterized by negative vorticity (Fig. 8(a)); a strain-dominated region is instead observed in the scour hole.

The dominance of strain rate is observed until the scour hole shows relatively steep walls and where a strong erosive action is observed. Instead, when the scour hole shows a relatively mild inclination and a stable formation of a wave jump has been observed (Fig. 9(a)), the dominance of the strain rate terms is greatly reduced (Fig. 9(b)).

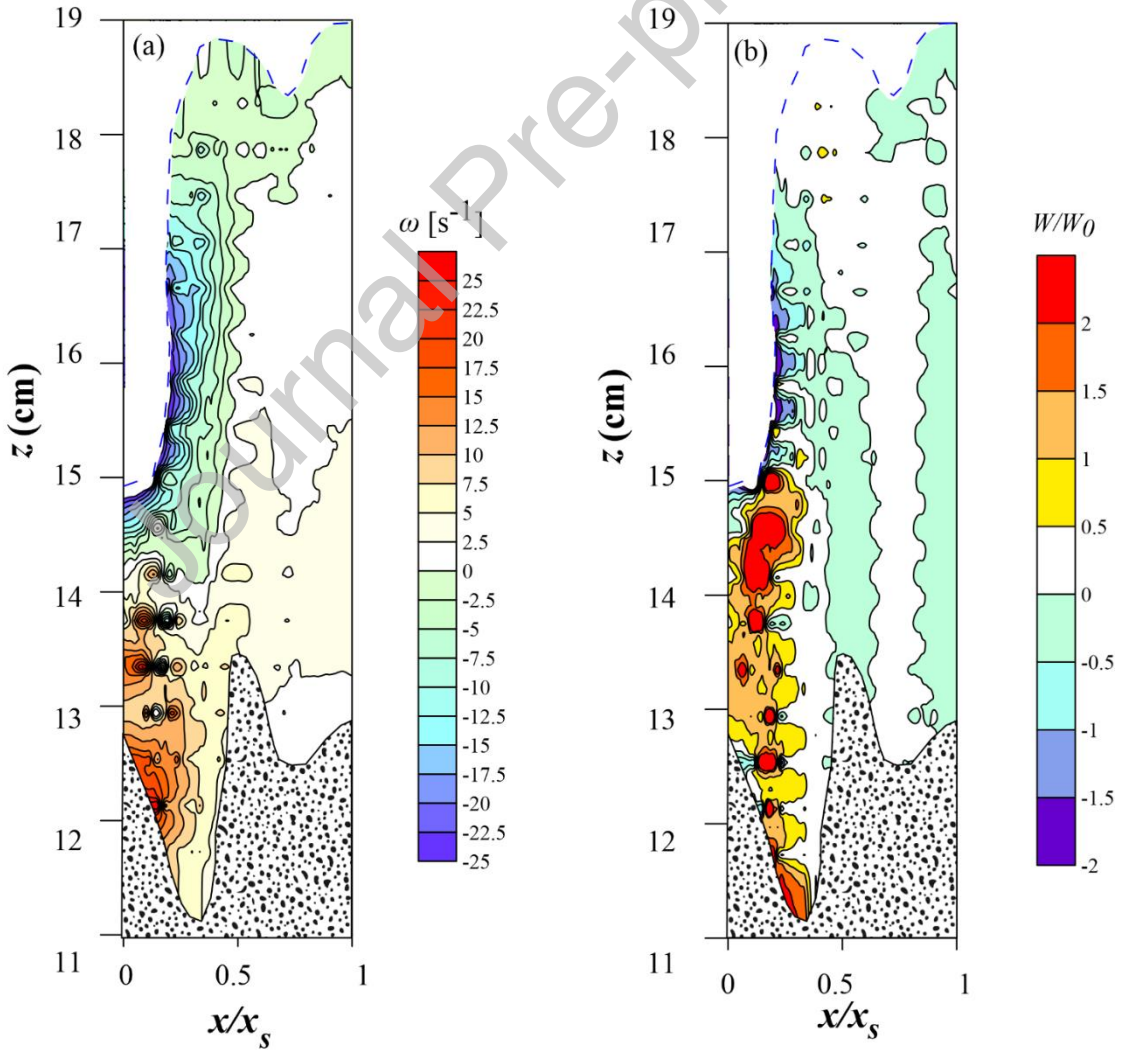

FIG. 8. Instantaneous map of (a) vorticity ω and of (b) W/W_0 at beginning of erosive action (t= 2s).

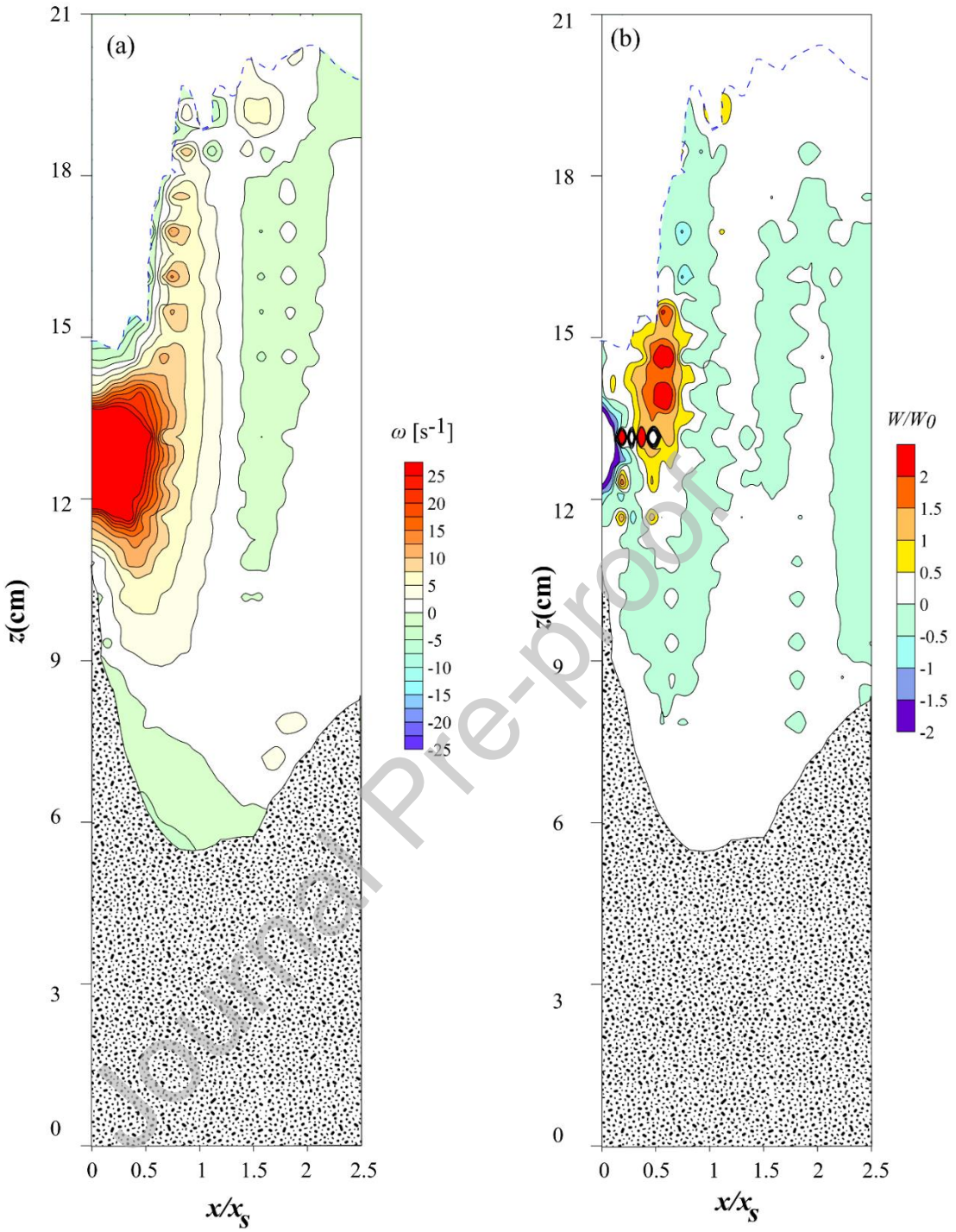

FIG. 9. Instantaneous map of (a) vorticity ω and of W/W_0 when the stable configuration has been reached (t=165s).

In order to better understand the behavior of the vorticity field at equilibrium configuration (Fig. 9(a)), the flow deceleration due to the convective term, $\widehat{U}_s \partial \widehat{U}_s / \partial s$ has been studied. As shown by Misra et al. (2008), the mean surface-parallel velocities have been calculated as:

$$\widehat{U}_s = U\cos\theta + V\sin\theta \tag{10}$$

where θ is the inclination of the mean surface on the horizontal.

Figure 10 shows the instantaneous map of the surface parallel convective acceleration when the stable configuration has been reached.

We observe that a flow deceleration occurs in the same location where a strong positive vorticity appears.

This is consistent with the observations made by Dabiry and Gharib (1997) that theoretically derived that that near-surface vorticity increases with increasing deceleration term.

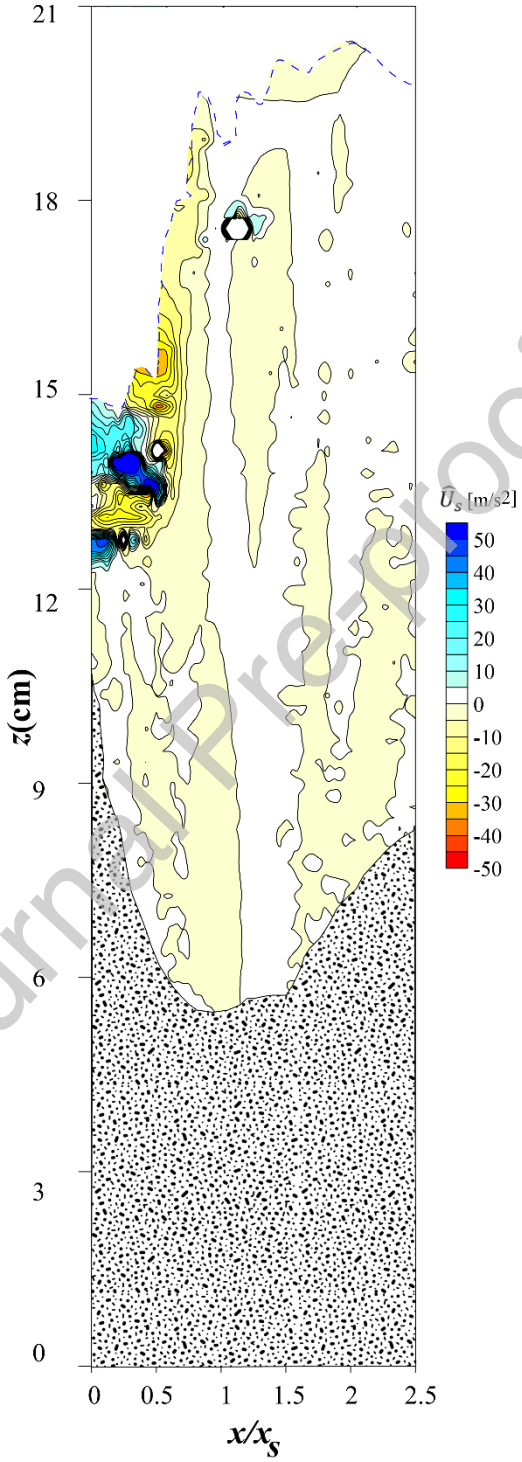

FIG. 10. Instantaneous map of the surface parallel convective acceleration when the stable configuration has been reached (t=165s).

3.3 Local scouring process characterization

Some experimental studies noticed a cyclic variation of jump types under specific flow conditions (Ohtsu and Yasuda, (1991); Mossa et al., 2002, Chanson and Toombes, (1998); Mossa et al., (1999, 2003)). The experiments by Abdel Ghafaret al. (1995) on local scour in sand-bed channel due to hydraulic jump showed that the hydraulic jump tended to repeat itself in a periodic form, from clockwise to anti-clockwise rotation of the vortex.

These results confirm the experimental findings by Mossa (1999), who showed that the oscillations of the hydraulic jump depended on the shape of the bed and on the hydrodynamic characteristics of the channel flow. In agreement with these observations, Figure 11 highlights that the configurations in which the oscillation between B and wave jump appears, occur along a boundary between the two regions of occurrence of each type. This boundary is represented by a log relation between the upstream Froude number $Fr_1 = U_1/\sqrt{gh_1}$ and the water depth ratio h_2/h_1.

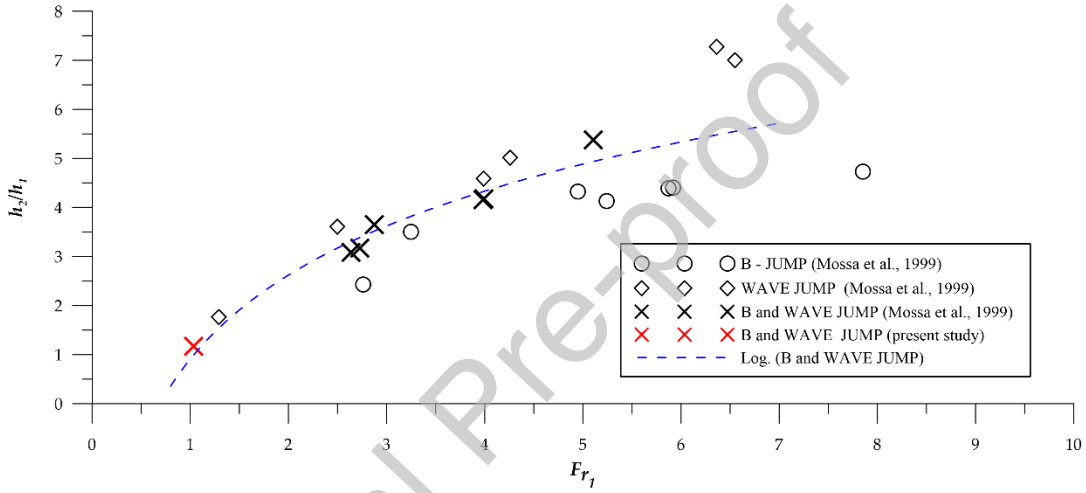

FIG. 11. Diagram of regions of occurrence for each jump type.

To understand the effect of oscillating hydraulic jumps on the scouring profiles, the calculated scouring profiles at different times are plotted in Fig. 12. The results obtained by the numerical model indicate that the maximum scour depth is almost constant after 160 s run time.

The results show that a strong horizontal erosive action tends to rapidly intensify when the system shifts from B to wave jump. Analyzing the instantaneous vorticity fields, the transition between the two jump types starts at *t*=63s and clearly ends at t= 65s. In fact, from t= 63s, Figure 12 shows a reduction in the vertical scour depth and a rapid increase in the horizontal scour depth.

Figure 13 reveals that three different phases of the scour process can be identified. Phase I, where the flow is characterized by a B-jump, shows a rapid increase of the scour to a depth which is more than 60% of the final depth, while the scour length increases at a much slower rate.

Phase II, when the transition between the two jump types has been observed, is dominated by a strong and fast increase of the horizontal dimension of the scour hole, while its depth decreases owing to the collapse of the upstream side.

Finally, during phase III a stable wave jump is observed, and the scour depth, length and volume all increase until equilibrium is reached.

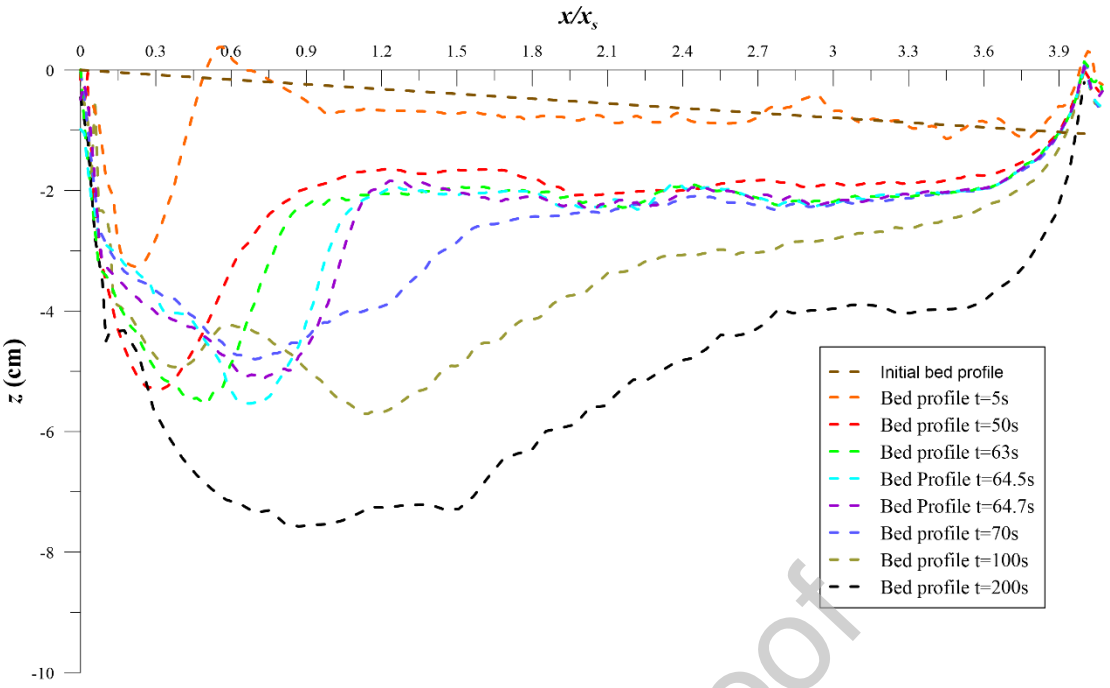

FIG. 12. Scour profiles of numerical model at different times

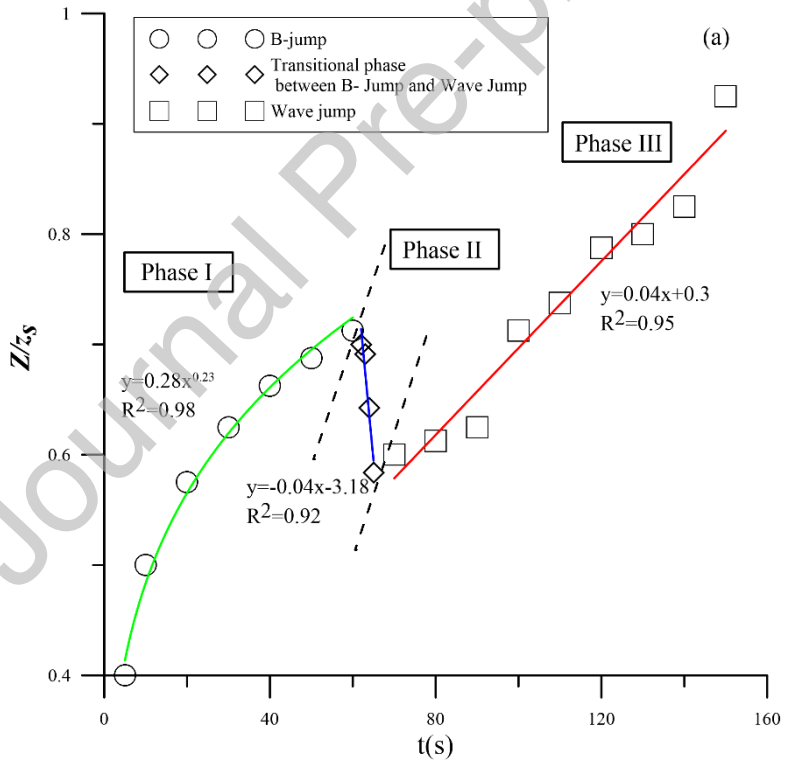

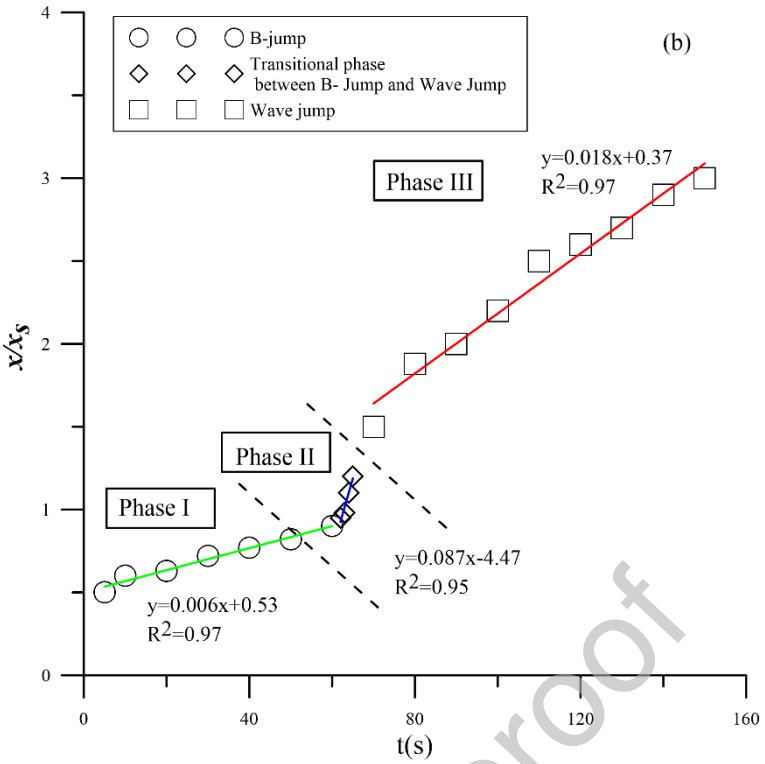

FIG. 13. Maximum (a) vertical and (b) horizontal scour profiles of numerical model at different times

4. Conclusions

The objective of the present work was to investigate the vorticity generation mechanism in a scour hole developed downstream of a grade control structure in sand-bed channels, providing a full hydrodynamic picture of the scouring process.

The liquid-granular flow has been simulated through a symplectic Weakly Compressible SPH (WCSPH) scheme with a two-equation turbulence model, where the two phases are treated as continua with different physical and rheological properties, in the hypothesis of solid transport mainly occurring as bed transport and of suspended solids only influencing the apparent viscosity of the liquid flow.

The SPH model was validated by comparing the simulated results with the experiments on the local scour holes downstream of hydraulic jump, showing that the simulations were consistent with experimental data.

As experimentally observed, our results indicate that three regions can be identified: the first is dominated by a jet-like flow characterized by high speed and plays a very important role in the downstream movement of sediments; the second is dominated by a clockwise local vortex at the position of maximum scour depth; third is dominated by a relatively aligned horizontal flow.

The detailed analysis of the turbulence characteristics in the scour hole at equilibrium conditions shows that both the maximum value of the streamwise and of the vertical turbulence intensities occur in the first region due to the jet flow. In the third region, there is a sharp reduction in turbulence intensity.

At equilibrium conditions, the stability of sediment particles is due to a significant decrease of turbulent energy production at the bed-flow interface.

The equilibrium configuration of flow field and bed topography is reached after a transitory period in which the system oscillates between two flow patterns: (i) the presence of a scour hole with a relatively steep hump downstream of it increases the free surface elevation and generates a B-jump type, characterized by a counterclockwise rotating macro-vortex structure (negative vorticity) which pushes the main flow towards the bed, where a strong erosive action is observed; (ii) the scour with a relatively modest inclination of the scour cavity leads to the formation of a wave jump dominated by a clockwise rotating macro-vortex structure (positive vorticity).

Furthermore, a cause-effect relation between near-surface flow deceleration and vorticity fluxes is detected, similarly to what observed in Dabiry and Gharib (1997).

The maps of the relative Okubo-Weiss parameter W/W_0 highlights the presence of coherent eddies ($W< 0$) in the region which exhibits negative vorticity near the surface; instead, a strain-dominated region is observed in the scour hole.

The dominance of strain rate is observed until the scour hole shows relatively steep walls and where a strong erosive action occurs. Instead, when the scour shows a relatively mild inclination and a stable wave jump forms, the dominance of the strain rate terms is greatly reduced.

Finally, the calculated scouring profiles at different times have been plotted to understand the effect of oscillating hydraulic jumps. These profiles show that the scour process evolves in three distinct phases: phase I, when the flow is characterized by a B-jump, shows a rapid increase of the scour to a depth which is more than 60% of the final depth, while the scour length increases at a much slower rate; phase II, when the transition between the two jump types takes place, is dominated by a strong and fast increase of the horizontal dimension of the scour hole, while its depth decreases owing to the collapse of the upstream side; phase III, when the flow is characterized by a stable wave jump and the scour depth, length and volume all increase until equilibrium is reached.

Author Contributions: D.D.P. and S.S. performed the numerical modelling; M.M. and M.B.M. performed the experiments; D.D.P., M.B.M., M.M. and S.S. analyzed the data; D.D.P. wrote the paper; M.B.M., M.M. and S.S. contributed suggestions, discussions and reviewed the manuscript. All authors have read and agreed to the published version of the manuscript.

Declaration of interests

The authors declare that they have no known competing financial interests or personal relationships that could have appeared to influence the work reported in this paper

Acknowledgment

The experiments were carried out at the Hydraulic Laboratory of the Mediterranean Agronomic Institute of Bari (Italy).

References

1. Amicarelli, A., Kocak, B., Sibilla, S., Grabe, J., 2017. A 3D smoothed particle hydrodynamics model for erosional dam-break floods. Int. J. Comput. Fluid Dyn. 31, 413–434.
2. Balachandar, R., Kells, J.A., 1997. Local channel in scour in uniformly graded sediments: The time-scale problem. Can. J. Civ. Eng. 24, 799–807.
3. Barile, S., De Padova, D., Mossa, M., Sibilla, S., 2020. Theoretical analysis and numerical simulations of turbulent jets in a wave environment. Phys. Fluids 32, 035105.
4. Bormann, N.E., Julien, P.Y., 1991. Scour downstream of grade-control structures. J. Hydraul. Eng. 117, 579–594.
5. Ben Meftah, M., Mossa, M., 2006. Scour holes downstream of bed sills in low-gradient channels. J. Hydraul. Res. 44, 497–509.
6. Ben Meftah, M.B., De Padova, D., De Serio, F., Mossa, M., 2021. Secondary currents with scour hole at grade control structures. Water (Switzerland), 13(3), 319. https://doi.org/10.3390/w13030319
7. Ben Meftah, M.B., De Serio, F., De Padova, D., Mossa, M., 2020. Hydrodynamic structure with scour hole downstream of bed sills. Water (Switzerland), 12(1), 186. https://doi.org/10.3390/w12010186.

8. Bertevas, E., Tran-Duc, T., Le-Cao, K., Khoo, B.C., Phan-Thien, N. 2019. A smoothed particle hydrodynamics (SPH) formulation of a two-phase mixture model and its application to turbulent sediment transport. Phys. Fluids 31, 103303.
9. Calderon-Sanchez, J., Martinez-Carrascal, J., Gonzalez-Gutierrez, L.M., Colagrossi, A.A., 2021. global analysis of a coupled violent vertical sloshing problem using an SPH methodology. Engineering Applications of Computational Fluid Mechanics 15(1), 865-888. https://doi.org/10.1080/19942060.2021.1921849
10. Carstens, M.R., 1966. Similarity laws for localized scour. J. Hydraul. Div. 92, 13–36.
11. Chang, Y.L., Oey, L.Y., 2014. Analysis of STCC eddies using the Okubo–Weiss parameter on model and satellite data. Ocean Dyn. 64, 259–271. https://doi.org/10.1007/s10236-013-0680-7
12. Chanson, H., Toombes, L., 1998. Supercritical flow at an abrupt drop: Flow patterns and aeration. Can. Jl of Civil Eng. 25(5), 956-966.
13. Dabiri, D., Gharib, M., 1997. Experimental Investigation of the vorticity generation within a spilling water wave. J Fluid Mech 330, 113–139.
14. D'Agostino, V., Ferro, V., 2004. Scour on alluvial bed downstream of grade-control structures. J. Hydraul. Eng. 130, 24–37.
15. De Padova, D., Mossa, M., Sibilla, S., Torti, E., 2013. 3D SPH modelling of hydraulic jump in a very large channel. J. Hydraul. Res. 51(2), 158–173.
16. De Padova, D., Dalrymple, R.A., Mossa, M., 2014. Analysis of the artificial viscosity in the smoothed particle hydrodynamics modelling of regular waves. J. Hydraul. Res. 52, 836–848.
17. De Padova, D., Mossa, M., Sibilla, S., 2016. SPH numerical investigation of the velocity field and vorticity generation within a hydrofoil induced spilling breaker. Environ. Fluid Mech. 16(1), 267–287.
18. De Padova, D., Mossa, M., Sibilla, S., 2017. SPH modelling of hydraulic jump oscillations at an abrupt drop. Water 9(10), 790. https://doi.org/10.3390/w9100790.
19. De Padova, D., Brocchini, M., Buriani, F., Corvaro, S., De Serio, F., Mossa, M., Sibilla, S., 2018a Experimental and numerical investigation of prebreaking and breaking vorticity within a plunging breaker. Water 10(4), 387. https://doi.org/10.3390/w10040387.
20. De Padova, D., Mossa, M., Sibilla, S., 2018b. SPH numerical investigation of characteristics of hydraulic jumps. Environ. Fluid Mech. 18(4), 849–870.
21. De Padova, D., Mossa, M., Sibilla, S., 2018c. SPH numerical investigation of the characteristics of an oscillating hydraulic jump at an abrupt drop. J. Hydrodyn. 30, 106.
22. De Padova, D., Mossa, M., Sibilla, S., 2019. Numerical investigation of the behaviour of jets in a wave environment. J. Hydraul. Res. 58, 618.
23. De Padova, D., Ben Meftah, M., De Serio, F., Mossa, M., Sibilla, S., 2020a. Characteristics of breaking vorticity in spilling and plunging waves. Environ. Fluid Mech. 20(2), 233–260.
24. De Padova, D., Mossa, M., 2020b. Modelling fluid–structure interactions: A survey of methods and experimental verification. Proc. Inst. Civ. Eng. 173, 159.
25. De Padova, D., Mossa, M., Sibilla, S., 2020c. Characteristics of nonbuoyant jets in a wave environment investigated numerically by SPH. Environ. Fluid Mech. 20(1), 189–202.
26. De Padova, D., Mossa, M., 2021. Multi-phase simulation of infected respiratory cloud transmission in air. AIP Advances 11(3). https://doi.org/10.1063/5.0047692.
27. Di Monaco, A., Manenti, S., Gallati, M., Sibilla, S., Agate G., Guandalini R., 2011. SPH Modeling of Solid Boundaries Through a SemiAnalytic Approach. Engineering Applications of Computational Fluid Mechanics 5(1), 1-15. https://doi.org/10.1080/19942060.2011.11015348.
28. Espa, P., Sibilla, S., Gallati, M., 2008. SPH simulations of a vertical 2-D liquid jet introduced from the bottom of a freesurface rectangular tank. Advances and Applications in Fluid Mechanics 3, 105–140.

29. Espa, P.; Sibilla, S., 2014. Experimental study of the scour regimes downstream of an apron for intermediate tailwater depths. J. Appl. Fluid Mech. 7, 611–624.
30. Federico, I., Marrone, S., Colagrossi, A., Aristodemo, F., Antuono, M., 2012. Simulating 2D open channel flows through an SPH model. Eur. J. Mech. B/Fluids 34, 35–46.
31. Fourtakas, G., Rogers, B.D., 2016. Modelling multi-phase liquid-sediment scour and resuspension induced by rapid flows using Smoothed Particle Hydrodynamics (SPH) accelerated with a graphics processing unit (GPU). Adv. Water Resour. 92, 186-199 https://doi.org/10.1016/j.advwatres.2016.04.009.
32. Fraccarollo L., Capart H., 2002. Riemann wave description of erosional dam-break flows. J. Fluid Mech. 461, 183–228.
33. Fu, L., Jin, Y.C., 2016. Improved multiphase Lagrangian method for simulating sediment transport in dam-break flows. J. Hydraul. Eng. 142 (6), 04016005.
34. Gaudio, R., Marion, A., Bovolin V., 2000. Morphological effects of bed sills in degrading rivers. J. Hydraul. Res. 38(2), 89–96.
35. Gingold, R.A., Monaghan, J.J., 1977. Smoothed particle hydrodynamics: Theory and application to nonspherical stars. Monthly Not. Royal Astron. Soc. 181, 375–389.
36. Hayashi, M., Gotoh, H., Sakai, T., Ikari, H., 2003. Lagrangian gridless model of toe scouring of seawall due to tsunami return flow. In: Proc. of Asia and Pacific coast, APAC, pp. 1–12.
37. Hilt, M., Roblou, R., Nguyen, C., Marchesiello, P., Lemarié, F., Jullien, S., Dumas, F., Debreu, L., Capet, X., Bordois, L., Benshila, R., Auclair, F., 2020. Numerical modeling of hydraulic control, solitary waves and primary instabilities in the Strait of Gibraltar. Ocean Modelling 155, 101642. 10.1016/j.ocemod.2020.101642. hal-02418114.
38. Khanpour, M., Zarrati, A.R., Kolandoozan, M., Shakibaeinia, A., Amirshahi, S.M., 2016. Mesh-free SPH modeling of sediment scouring and flushing. Comput. & Fluids 129, 67–78.
39. Launder, B.E., Spalding, D.B., 1974. The numerical computation of turbulent flows. Comput. Methods Appl. Mech. Eng. 3, 269–289.
40. Lenzi, M.A., Marion, A., Comiti, F., Gaudio R., 2002. Local scouring in low and high gradient streams at bed sills, J. Hydraul. Res., 40(6), 731–739.
41. Lin, P., Liu X., Zhang J., 2015. The simulation of a landslide-induced surge wave and its overtopping of a dam using a coupled ISPH model. Engineering Applications of Computational Fluid Mechanics, 9(1), 432-444. https://doi.org/10.1080/19942060.2015.1048620.
42. López, D., Marivela, R., Garrote, L., 2010. Smoothed particle hydrodynamics model applied to hydraulic structures: A hydraulic jump test case. J. Hydraul. Res. 48, 142–158.
43. Lu, J.Y., Hong, J.H., Chang, K.P., Lu, T.F., 2013. Evolution of scouring process downstream of grade-control structures under steady and unsteady flows. Hydrol. Process. 27, 2699–2709.
44. Lucy, L., 1997. A numerical approach to the testing of fusion process. Astronom. J. 82(12), 1013–1024.
45. Martín-Vide, J.P., Andreatta A., 2006. Disturbance caused by bed sills on the slopes of steep streams. J. Hydraul. Eng., 132(11), 1186–1194.
46. Makris, C.V., Memos, C.D., Krestenitis, Y.N., 2016. Numerical modeling of surf zone dynamics under weakly plunging breakers with SPH method. Ocean Modell. 98, 12–35.
47. Manenti, S., Pierobon, E., Gallati, M., Sibilla, S., D'Alpaos, L., Macchi, E., Todeschini, S., 2016. Vajont disaster: smoothed particle hydrodynamics modeling of the postevent 2D experiments. J. Hydraul. Eng. 142(4), 05015007.
48. Manenti, S., Sibilla, S., Gallati, M., Agate, G., Guandalini, R., 2012. SPH simulation of sediment flushing induced by a rapid water flow. J. Hydraul. Eng. 138, 272–284.
49. Manenti, S., Wang, D., Domínguez, J.M., Li, S., Amicarelli, A., Albano, R., 2019. SPH Modeling of Water-Related Natural Hazards. Water 11(9), 1875. https://doi.org/10.3390/w11091875.

50. Manes, C., Brocchini, M., 2015. Local scour around structures and the phenomenology of turbulence. Journal of Fluid Mechanics 779, 309-324. https://doi.org/10.1017/jfm.2015.389.
51. Mattioli, M., Alsina, J.M., Mancinelli, A., Miozzi, M., Brocchini, M. 2012. Experimental investigation of the nearbed dynamics around a submarine pipeline laying on different types of seabed: The interaction between turbulent structures and particles. Advances in Water Resources 48, 31-46. https://doi.org/10.1016/j.advwatres.2012.04.010.
52. Meister, M., Rauch, W., 2016. Wastewater treatment modelling with smoothed particle hydrodynamics. Environmental Modelling & Software 75, 206-211.
53. Misra, S.K., Kirby, J.T., Brocchini, M., Veron, F., Thomas, M., Kambhamettu, C., 2008. The mean and turbulent flow structure of a weak hydraulic jump. Phys. Fluids 20, 035106. https://doi.org/10.1063/1.2856269.
54. Monaghan, J.J., 1992. Smoothed particle hydrodynamics. Annu. Rev. Astron. Astrophys. 30, 543–574.
55. Mossa, M., 1999. On the oscillating characteristics of hydraulic jumps. J. Hydraul. Res. 37(4), 541-558.
56. Mossa, M., Petrillo, A., Chanson, H., 2003. Tailwater Level Effects on Flow Conditions at an Abrupt Drop. J. Hydraul. Res. 41, 39–51.
57. Okubo, A., 1970. Horizontal dispersion of floatable particles in the vicinity of velocity singularities such as convergences. Deep-Sea Res 17, 445–45.
58. Ohtsu, I., Yasuda, Y., 1991.Transition from supercritical to subcritical flow at an abrupt drop. J. Hydraul. Res. 29(3), 309-328.
59. Papanicolaou, A.N., Bressan, F., Fox, J., Kramer, C., Kjos, L., 2018. Role of structure submergence on scour evolution in gravel bed rivers: Application to slope-crested structures. J. Hydraul. Eng. 144, 1087–1093.
60. Pahar, G., Dhar, A., 2017. Coupled incompressible smoothed particle hydrodynamics model for continuum-based modelling sediment transport. Adv. Water Resour. 102, 84–98.
61. Jonsson, P., Andreasson, P., J.Gunnar I. Hellström, Jonsén, P., Staffan Lundström, T., 2016. Smoothed Particle Hydrodynamic simulation of hydraulic jump using periodic open boundaries. Applied Mathematical Modelling 40(19-20), 8391-8405.
62. Pu, J.H., Shao, S., Huang Y., Hussain K., 2013. Evaluations of SWEs and SPH Numerical Modelling Techniques for Dam Break Flows. Engineering Applications of Computational Fluid Mechanics 7(4), 544-563. https://doi.org/10.1080/19942060.2013.11015492.
63. Ran, Q.H., Tong, J., Shao, S.D., Fu, X.D., Xu, Y.P., 2015. Incompressible SPH scour model for movable bed dam break flows. Adv. Water Resour. 82, 39–50.
64. Sibilla, S., 2015. An algorithm to improve consistency in smoothed particle hydrodynamics. Comput. Fluids. 118, 148–158.
65. Shi, H., Yu, X., Dalrymple, R.A., 2017. Development of a two-phase SPH model for sediment laden flows. Comput. Phys. Commun. 221, 259-272. https://doi.org/10.1016/j.cpc.2017.08.024.
66. Tregnaghi, M., Marion, A., Gaudio, R., 2007. Affinity and similarity of local scour holes at bed sills. Water Resour. Res. 43, W11417. http://hdl.handle.net/11577/1774833.
67. Ulrich, C., Rung, T., Leonardi, M., 2013. Multi-physics SPH simulation of complex marine-engineering hydrodynamic problems. Ocean Engineering 62, 109-121.
68. Wang, D., Li, S.W., Arikawa, T., Gen, H.Y., 2016. ISPH simulation of scour behind seawall due to continuous tsunami overflow. Coast. Eng. J. 58(3), 1650014.
69. Wang, L., Melville, B.W., Guan, D., Whittaker, C.N., 2018. Local scour at downstream sloped submerged weirs. J. Hydraul. Eng. 144, 04018044.
70. Weiss, J., 1991. The dynamics of enstrophy transfer in two-dimensional hydrodynamics. Physica D: Nonlinear Phenomena 48(2-3), 273–294. https://doi.org/10.1016/0167-2789(91)90088-Q.

71. Wendland, H., 1995. Piecewise polynomial, positive definite and compactly supported radial functions of minimal degree. Adv. Comput. Math. 4, 389–396.
72. Willmott, C.J., 1981. On the validation of models. Phys. Geogr. 2, 184–194.
73. Xie, J., Jin Y.C., 2016. Parameter determination for the Cross rheology equation and its application to modeling non-Newtonian flows using the WC-MPS method. Engineering Applications of Computational Fluid Mechanics 10(1), 111-129.
74. Xia, X. , Liang, Q., 2016. A GPU-accelerated smoothed particle hydrodynamics (SPH) model for the shallow water equations. Environ. Model. Softw. 75, 28-43.
75. Wang, D., Shao, S., Li, S., Shi, Y., Arikawa, T; Zhang,H., 2018. 3D ISPH erosion model for flow passing a vertical cylinder. Journal of Fluids and Structures 78, 374-399.
76. Zheng, Xg., Chen, R., Luo, M., Kazemi E., Liu., X., al., 2019. Dynamic hydraulic jump and retrograde sedimentation in an open channel induced by sediment supply: experimental study and SPH simulation. J. Mt. Sci. 16, 1913–1927. https://doi.org/10.1007/s11629-019-5397-8.
77. Zubeldia, E. H., Fourtakas, G., Rogers, B.D., Farias, M.M., 2018. Multi-phase SPH model for simulation of erosion and scouring by means of the shields and Drucker–Prager criteria. Advances in Water Resources 117, 98-114.